Controlling the Twin Drive by decoupling

Citation for published version (APA):
Best, de, J. J. T. H. (2004). *Controlling the Twin Drive by decoupling*. (DCT rapporten; Vol. 2004.093). Technische Universiteit Eindhoven.

Document status and date:
Published: 01/01/2004

Document Version:
Publisher's PDF, also known as Version of Record (includes final page, issue and volume numbers)

Please check the document version of this publication:

• A submitted manuscript is the version of the article upon submission and before peer-review. There can be important differences between the submitted version and the official published version of record. People interested in the research are advised to contact the author for the final version of the publication, or visit the DOI to the publisher's website.
• The final author version and the galley proof are versions of the publication after peer review.
• The final published version features the final layout of the paper including the volume, issue and page numbers.

Link to publication

General rights
Copyright and moral rights for the publications made accessible in the public portal are retained by the authors and/or other copyright owners and it is a condition of accessing publications that users recognise and abide by the legal requirements associated with these rights.

- Users may download and print one copy of any publication from the public portal for the purpose of private study or research.
- You may not further distribute the material or use it for any profit-making activity or commercial gain
- You may freely distribute the URL identifying the publication in the public portal.

If the publication is distributed under the terms of Article 25fa of the Dutch Copyright Act, indicated by the "Taverne" license above, please follow below link for the End User Agreement:

www.tue.nl/taverne

Take down policy
If you believe that this document breaches copyright please contact us at:

openaccess@tue.nl

providing details and we will investigate your claim.

Download date: 16. Nov. 2023

Controlling the Twin Drive by decoupling

J.J.T.H. de Best
0496284

Report No. DCT 2004.93

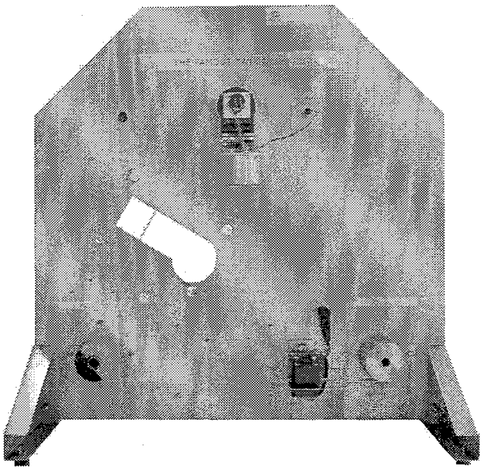

Internal traineeship

Coaches:	dr. ir. P.F. Lambrechts
	ir. M.L.G. Boerlage
Supervisor:	prof.dr.ir. M.Steinbuch

EINDHOVEN UNIVERSITY OF TECHNOLOGY
DEPARTMENT OF MECHANICAL ENGINEERING
CONTROL SYSTEM TECHNOLOGY GROUP

Summary

Many industrial motion systems are MIMO systems which possess coupling between inputs and outputs. These coupled MIMO systems are difficult to control and therefore there is a strong need in developing control design methodes for industrial multivariable motion control problems. In this work it is investigated whether or not it is possible to decouple the dynamics of the Twin Drive, so that controllers can be designed for this decoupled system.

In order to achieve this, the Twin Drive is connected to a data acquisition system. Hereafter experiments are carried out to identify the system, which includes the calibration of the tachos, determination of the motor constants, estimation of motor parameters and the measurement of frequency response functions in three experimental cases.

With the identified system, a control design is presented based on decoupling of the dynamics. A modal analysis is performed from which the system is transformed into natural coordinates leading to a decoupling of the dynamics. In order to quantify the residual non-diagonal terms compared to the diagonal terms the relative gain array (RGA) has been computed which shows that the diagonal terms dominate and the system has little coupling. In this way, two independent SISO controllers are designed to control the Twin Drive.

The main conclusion of this work is that by modal decoupling of the Twin Drive, the characteristic loci of the multivariable system can be manipulated by means of classical SISO loopshaping techniques. Hence, stability of multivariable electromechanical systems can be obtained. The bandwidth of the MIMO system is 30 $[Hz]$, which is ten times higher than the systems first resonance frequency.

Further investigation is recommended concerning the velocity dependency of the dynamics. Also the slipping behaviour on the rolls should be studied, as this affects the damping of the system. An interesting case would be to control the velocity of the toproll together with the belt tensions.

Nomenclature

Symbols:

Symbol	**Quantity**	**Unit**
C	Controller	-
$\underline{D}$	Damping matrix	-
$\underline{D}^{\star}$	New damping matrix	-
d	Viscous damping factor	$[Nms/rad]$
$d^{\star}$	New viscous damping factor	$[Nms/rad]$
$\lceil d_r \rfloor$	Normalized damping matrix	-
e	Error	$[rad]$ or $[rad/s]$
E_{emf}	Back-emf	$[V]$
f	Frequency	$[Hz]$
$\underline{G}$	Square matrix	-
$\underline{\eta}$	Column of natural coordinates	-
$\underline{\dot{\eta}}$	Column of natural velocities	-
$\underline{\ddot{\eta}}$	Column of natural accelerations	-
H	Transfer	-
i	Current	$[A]$
J	Inertia	$[kgm^2]$
k	Dry friction coefficient	$[Nm]$
k	Stiffness	$[Nm/rad]$
$\underline{K}$	Stiffness matrix	-
k_m	Motor constant	$[Nm/A]$
$\lceil k_r \rfloor$	Normalized stiffness matrix	-
$\underline{\Lambda}$	Relative Gain Array (RGA)	-
L	Inductance	$[Henry]$
$\underline{M}$	Mass matrix	-
$\lceil m_r \rfloor$	Normalized mass matrix	-
ξ_r	Dimensionless damping coefficient	-
$\underline{N}$	Input column	-
$\underline{P}$	Transfer function matrix	-
$\underline{P}_{modal}$	Modal transfer function matrix	-
n	noise	-

Table 1: List of symbols

Symbol	**Quantity**	**Unit**
$\underline{q}$	Column of physical coordinates	-
$\underline{Q}$	Input column	-
R	Resistance	$[\Omega]$
S	Sensitivity	-
σ	Standard deviation	-
T	Torque input	$[Nm]$
t	Time	$[s]$
τ	Time constant	-
u	Input	$[V]$ or $[Nm]$
$\underline{u}$	Input column	$[Nm]$
v	Voltage	$[V]$
ϕ	Angle of rotation	$[rad]$
$\dot{\phi}$	Rotational speed	$[rad/s]$
$\ddot{\phi}$	Rotational acceleration	$[rad/s^2]$
ω	Rotational speed	$[rad/s]$

Subscript

Symbol	**Quantity**	**Unit**
0	Initial condition	-
1	Motor 1	-
2	Motor 2	-
3	Toproll	-
12	From motor 1 to motor 2	-
13	From motor 1 to toproll	-
23	From motor 2 to toproll	-

Contents

Summary i

Nomenclature iii

1 Introduction 1
- 1.1 Problem statement and objective 1
- 1.2 Outline 2

2 Twin Drive Setup 3
- 2.1 Geometry 3
- 2.2 Actuation and Measurements 4

3 System Identification 5
- 3.1 Offset tachos 5
- 3.2 Calibration tachos 6
- 3.3 Motor constants 6
- 3.4 Parameter estimation 8
- 3.5 Frequency Response Functions (FRF) 11
  - 3.5.1 Case I 12
  - 3.5.2 Case II 13
  - 3.5.3 Case III 15
- 3.6 Conclusions 17

4 Control Design 19
- 4.1 Model Fitting 19
- 4.2 Modal Analysis 20
- 4.3 Modal Decoupling 21
- 4.4 Control Design 24
- 4.5 Conclusions 27

5 Conclusion and Recommendations 29
- 5.1 Conclusions 29
- 5.2 Recommendations 30

A Linearized Models 31
- A.1 Fourth Order Model 31
- A.2 Sixth order model 32

B Experimental Results **35**
B.1 Offset tachos 35
B.2 Calibration tachos 36
B.3 Motor constants 37
B.4 Parameter estimation 37
B.5 Frequency Response Functions 38

C Control Design **41**

Bibliography **49**

Chapter 1

Introduction

In the production of steel plates the main process is rolling. By rolling a block of steel the thickness decreases while the length of the plate increases. This process cannot be done in one operation. The plate has to be rolled several times. By doing so the rolling mills have to turn harder each time the plate gets thinner along the process. If the velocities of these rolls are not well synchronized, the plate can break or the plate can start to pile up. By controlling the tensile force of the plate and the velocities of the rolls after each rolling operation, these problems can be avoided.

The problem sketched above is a typical MIMO (Multi Input Multi Output) control problem. At Corus [Har04] an experimental setup has been constructed in order to demonstrate this. We will refer to this setup as the Twin Drive. With the Twin Drive the MIMO control problem can be demonstrated.

1.1 Problem statement and objective

To demonstrate the MIMO control problem a model can be derived for the Twin Drive. With this model, several controllers can be designed based on different methods. This leads to the long term objective:

To develop control design methodes for industrial multivariable motion control problems.

In this work, we will limit ourselves to the following problem statement:

Is it possible to decouple the dynamics of the Twin Drive and can controllers be designed for this decoupled system?

Before this can be achieved, the Twin Drive has to be connected to a data acquisition system. Also a model will be derived for the Twin Drive. It will be investigated how and up to what degree the system can be decoupled. Finally, a controller is designed.

1.2 Outline

First the experimental environment of the Twin Drive is described in Chapter 2. Chapter 3 explains the experiments and discusses the results of these experiments. Chapter 4 includes the modal analysis and the modal decoupling of the system. Also the controller is designed in this chapter. The report ends with conclusions and recommendations.

Chapter 2

Twin Drive Setup

In this chapter the Twin Drive setup will be described. The first section involves the geometry of the Twin Drive. The next section, all devices which are needed to control the Twin Drive will be presented.

2.1 Geometry

In this section the geometry of the Twin Drive will be given. A schematic representation of the Twin Drive is given in Figure 2.1.

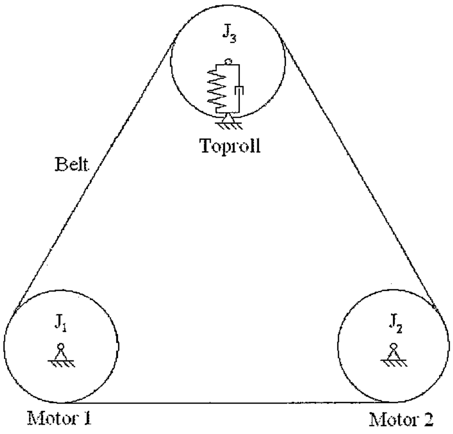

Figure 2.1: Schematic representation Twin Drive

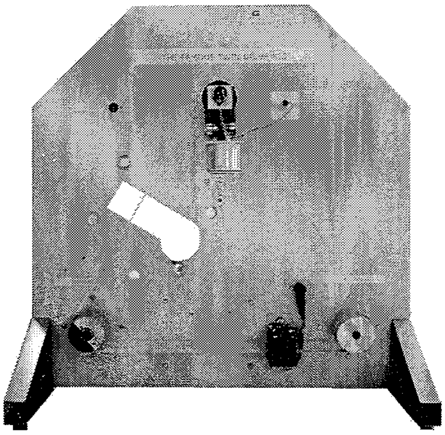

Figure 2.2: Twin Drive

The Twin Drive consists of three rolls which form an equiangular triangle. The two lower rolls are fixed. The toproll (see Figure 2.1), supported by a spring and damper, can move in vertical direction. The stiffness of the spring that is connected to the toproll is very large so that the deviation of the toproll with respect to its original position is negligible (max 3 [*mm*]) compared to the distance of the toproll and one of the two lower rolls (405 [*mm*]).

2.2 Actuation and Measurements

With the given geometry, the next step is to connect the Twin Drive to a data acquisition system. This section describes the actuation and measurement devices that the Twin Drive contains and how these are connected. The total setup of the Twin Drive is schematic represented in Figure 2.3.

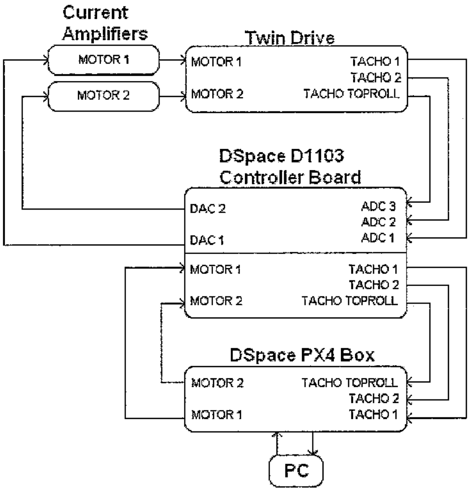
Current Amplifiers
MOTOR 1
MOTOR 2
Twin Drive
MOTOR 1
MOTOR 2
TACHO 1
TACHO 2
TACHO TOPROLL
DSpace D1103 Controller Board
DAC 2
DAC 1
ADC 3
ADC 2
ADC 1
MOTOR 1
MOTOR 2
TACHO 1
TACHO 2
TACHO TOPROLL
DSpace PX4 Box
MOTOR 2
MOTOR 1
TACHO TOPROLL
TACHO 2
TACHO 1
PC

Figure 2.3: Schematic representation setup

The two lower rolls are actuated by DC motors. These motors have tachos and the voltage can be measured, which is a measure for the angular velocity ω_1 and ω_2 respectively. The toproll is an idle roll. This roll cannot be actuated. ω_3 can be measured by means of a tacho mounted on the toproll. The toproll is fixed to a load cell so that the vertical force, acting on this roll, can be measured. However the amplifier for measuring the voltage of this load cell was not available so this sensor is not used in this work.

The whole setup is connected to the data acquisition system DSpace. This data acquisition system consist of DAC's (Digital to Analog Converters) and ADC's (Analog to Digital Converters). The actual controller is exported from the PC on to the PX4 Box (see Figure 2.3). With the DAC's a voltage can be applied to the current amplifiers. The dynamics of the current amplifiers are considered to be high frequent (order of 1-10 $[kHz]$) compared to the bandwidth of the system (order of 0.1-10 $[Hz]$). Therefore the amplifier is assumed to be ideal for frequencies of interest. With this assumption the relation between the voltage and the current is a constant factor 2 $[-]$.

Chapter 3

System Identification

In order to control the Twin Drive, a model is required. Therefore the objective of this chapter is to obtain a model for the Twin Drive. The following sections describe the steps that are taken to obtain this model.

First a compensation is made for the offsets of the ADC's to obtain the correct measurement. After this, experiments are carried out in order to determine all system variables. This includes the calibration of the tachos and the determination of the motor constants. In section 3.4 parameters of the two motors of the Twin Drive have been estimated that are used to fit the model. Finally, different kinds of FRF's (Frequency Respones Functions) are measured from which the model of the Twin Drive is derived.

3.1 Offset tachos

During the first experiment the offsets of the ADC's of the data acquisition system have been determined in order to compensate them to obtain the correct angular velocity.
When the whole system is in rest (i.e. the motors are not actuated) the output voltage of all three tachos have been measured. From the data the mean offsets have been determined. After five experiments, the mean is determined as given in the following table:

Offset	mean $[V]$	3σ $[V]$
Motor 1	$9.0 \cdot 10^{-5}$	$9.9e \cdot 10^{-6}$
Motor 2	$1.0 \cdot 10^{-4}$	$1.1e \cdot 10^{-5}$
Toproll	$1.1 \cdot 10^{-4}$	$1.4e \cdot 10^{-5}$

Table 3.1: Offsets of the tachos

In the future these offsets can be compensated for, performing a small experiment as described above to obtain the correct angular velocity. In Appendix B.1 all measured offsets are given.

3.2 Calibration tachos

After having compensated the offsets, the tachos are calibrated. The following experiment describes for each tacho how to get the angular velocity ω in radians per second instead of voltages. For the two motors the same experiment is carried out. On top of the roll a mark is made. Driving the angular velocity to a steady state value the roll is enlightened with a stroboscoop. By decreasing the frequency of the stroboscoop the mark can be visualized as a spot that is standing still. In that case the frequency of the stroboscoop equals the number of revolutions of the roll. At the same time the voltage of the tacho can be measured. This is done for several (positive and negative) angular velocities. Now a relation can be obtained between the voltage of the tacho and the actual angular velocity. For calibration of the tacho of the toproll the belt is wrapped around the three rolls and the torque is applied to one of the motors. The result of the tacho of motor 1 is given in Figure 3.1. The result of the other tachos are given in Appendix B.2.

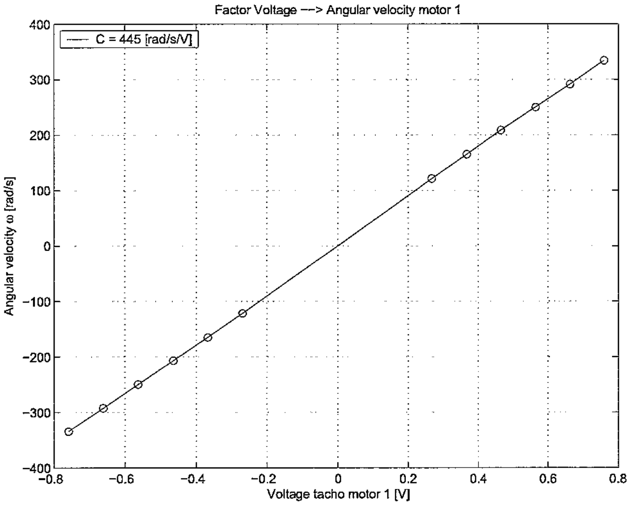

Figure 3.1: Factor voltage to radians per second motor 1

From Figure 3.1 it can be concluded that the angular velocity is a linear function of the voltage of the tacho. Therefore a linear fit is made described by the function

$$\omega = CV \tag{3.1}$$

where V denotes the measured voltage and ω denotes the measured angular velocity. The coefficient C that describes this linear relation is 445 $[rad/s/V]$. For the tachos of motor 2 and the toproll the same linear relations holds. The factor for motor 2 is 444 $[rad/s/V]$. For the toproll this factor equals 617 $[rad/s/V]$.

3.3 Motor constants

The inputs of the Twin Drive are voltages which are transformed into a torque that is applied to the motor. The next experiment is to determine the relations between the current that is applied to the motor and the torque it produces. Therefore the results of the previous experiments were necessary. A model of the DC motor [Mohan02] is given in Figure 3.2.

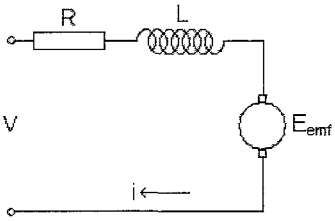

Figure 3.2: Model of DC motor

The following relationship holds for this model:

$$v = Ri + L\frac{\partial i}{\partial t} + E_{emf} \tag{3.2}$$

The above equation describes a DC motor that is driving a load. Another possibility is that the DC motor is mechanically driven by an other power source. In that case the DC motor functions like a generator. Measuring the voltage at the input of the DC motor (i.e. the output when functioning like a generator) results in a current loop which is not closed, because of the high internal resistance. Therefore no current will flow. What can be measured is the back-EMF, E_{emf}. Having calibrated the tachos, the angular velocity ω also can be measured. Using equations 3.3 and 3.4 the motor constant can be determined.

$$T = k_m I \tag{3.3}$$

$$E_{emf} = k_m \omega \tag{3.4}$$

In practice, motor 1 is driven by motor 2 to determine the motor constant of motor 2. To determine the motor constant of motor 2, motor 2 is driven by motor 1.

Figure 3.3 shows the measured data for determining the motor constant for motor 1.

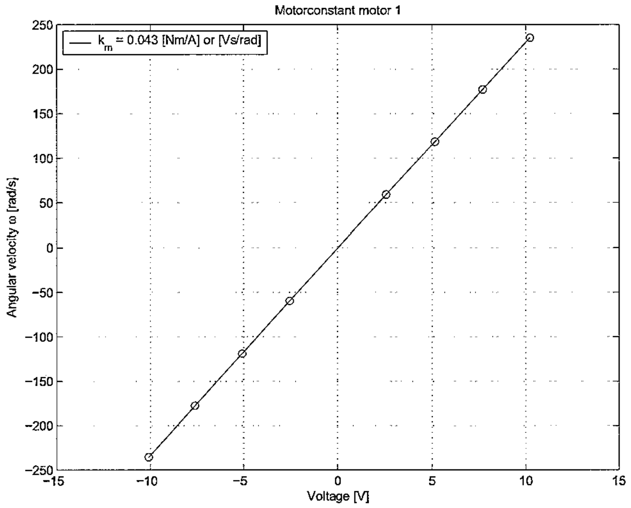

Figure 3.3: Motor constant motor 1

It can be concluded that there exists a linear relationship between the measured voltage and the measured angular velocity. The motor constant for motor 1 follows from the linear fit: $4.3 \cdot 10^{-2}$ $[Nm/A]$. The motor constant for motor 2 is $4.4 \cdot 10^{-2}$ $[Nm/A]$. For the experimental data of the motor constant of motor 2 see Appendix B.3.

3.4 Parameter estimation

With the results of sections 3.2 and 3.3 the system variables are determined. In this section three parameters of the motors are estimated: the coulomb friction factor, the inertia and the viscous damping factor. These parameters will be used to fit the experimental data with the model. The equation of motion of the motor is given below:

$$J\ddot{\phi} + d\dot{\phi} + ksign(\dot{\phi}) = T \tag{3.5}$$

First the coefficient k, representing the coulomb friction $[Nm]$, has been determined. A torque is applied to the motor in such a way that it nearly overcomes the coulomb friction. The experiment has been carried out several times for both rotational directions. The result of this experiment is that for positive direction, the value of k for motor 1 is 0.024 $[Nm]$. For negative direction this value equals -0.023 $[Nm]$. For motor 2 these values are 0.028 $[Nm]$ and -0.026 $[Nm]$ respectively. It can be concluded that the dry friction is not symmetric for the two directions what might be caused by the orientation of the brushes of the motor. Also during the measurements the dry friction was varying, what might be caused by temperature dependency of the lubrication of the bearings.

To determine the inertia J and the viscous damping factor d, step responses of the velocities have been measured. A torque is applied to obtain a constant angular velocity. Then every 20 seconds a constant amount of torque is added. The torque and the velocity are measured. One of these measurements are given in Figure 3.4.

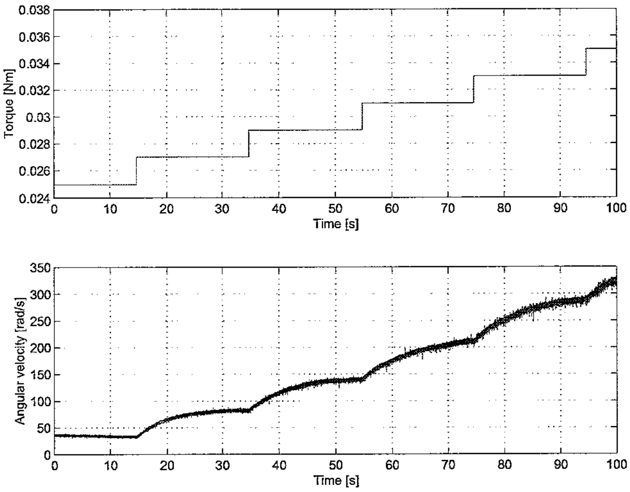

Figure 3.4: Input and output of parameter estimation

The angular velocity shows a first order response every 20 seconds. Writing the equation of motion above in terms of angular velocity ($\dot{\phi} = \omega$) and by defining $T_{dry} = ksign(\dot{\phi})$ results in:

$$J\dot{\omega} + d\omega = T - T_{dry} = T_{new} \tag{3.6}$$

The transfer function between the velocity ω and input T_{new} of the above equation in Laplace domain with $K = \frac{1}{d}$ and $\tau = \frac{J}{d}$ is:

$$\frac{K}{\tau s + 1} \tag{3.7}$$

The solution of the step response of ω in time domain is:

$$\omega = \omega_0 + K(1 - e^{\frac{-t}{\tau}}) \tag{3.8}$$

For each step the above response can be fitted on the experimental data, see Figure 3.5.

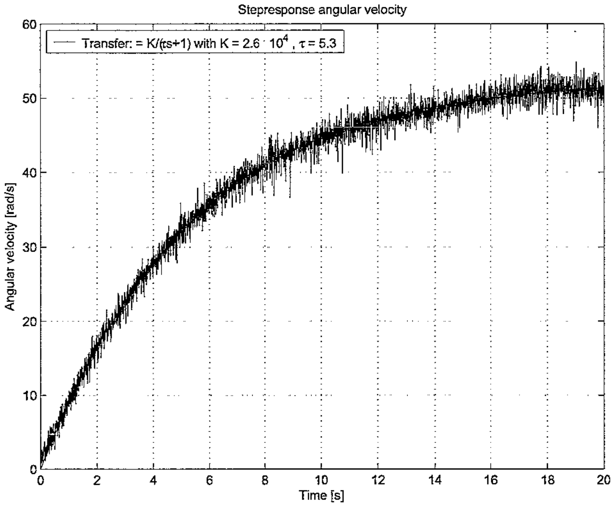

Figure 3.5: Fit on experimental data

This is done by using the optimization algorithm `fminunc` of MATLAB. This algorithm minimizes the following cost function:

$$\min_{K,\tau}\left\{\sum_{i=1}^{n}\left(K\left(1-e^{\frac{-t_i}{\tau}}\right)-m_i\right)^2\right\} \tag{3.9}$$

where m_i is a sample of the measured time response. Each step, an estimation of the parameters J an d can be made. The experiment is done ten times with four steps every experiment with different directions. The results are given below:

Estimated parameters	$J[kgm^2]$	$3\sigma(J)[kgm^2]$	$d[Nms/rad]$	$3\sigma(d)$
Motor 1	$2.1 \cdot 10^{-4}$	$6.0 \cdot 10^{-5}$	$3.3 \cdot 10^{-5}$	$1.7 \cdot 10^{-5}$
Motor 2	$2.0 \cdot 10^{-4}$	$8.3 \cdot 10^{-5}$	$4.6 \cdot 10^{-5}$	$4.3 \cdot 10^{-5}$

Table 3.2: Parameters J and d

The 3σ value of the damping constant d is very large. The value of d is hard to estimate. When it comes to controlling the motor, the uncertain viscous damping is not a problem. For low frequencies this leads to phase lead.

3.5 Frequency Response Functions (FRF)

To obtain a model of the Twin Drive, Frequency Response Functions have been measured. This section explains how these FRF's have been measured and the results are given and discussed. The following FRF's have been measured: the transfer functions of the two motors without the belt (I), the four transfer functions with the belt wrapped around the two motors (II) and the transfer functions from the motors to the toproll for both the rotational directions (III), see Figure 3.6.

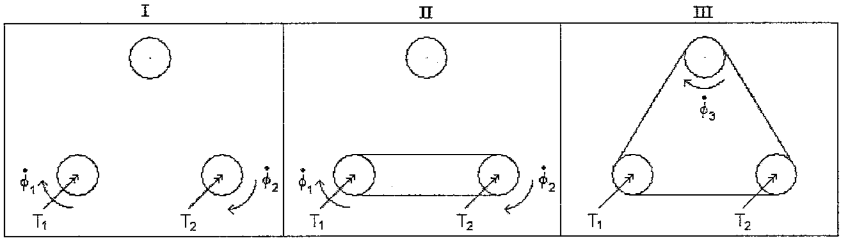

Figure 3.6: Measured transfer functions

To obtain the FRF of the process, the sensitivity has been measured. This can be done by injecting noise n between the controller and the proces (see Figure 3.7). At the same time this noise is measured together with the plant input w. The transfer function from n to w is the sensitivity: $S = \frac{1}{1+CP}$. By doing a fourier transformation on the time signals n and w, this transfer can be determined. Together with the known controller which is used for this measurement the FRF of the proces can be determined: $P = (S^{-1} - 1)C^{-1}$.

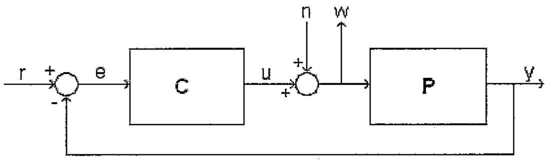

Figure 3.7: Sensitivity measurement

This has been implemented in DSpace. The total measuring time is 100 seconds. Therefore the lowest frequency that can be measured is 0,01 $[Hz]$ with a frequency resolution of 0,01 $[Hz]$. The sample rate during the experiment is 2 $[kHz]$ so that the highest frequency that can be measured, the Nyquist frequency, is 1 $[kHz]$.

The FRF's have been validated by doing the same measurement with SigLab, which has advantages concerning the signal conditioning. The setup for measuring the FRF with SigLab is given in Figure 3.8.

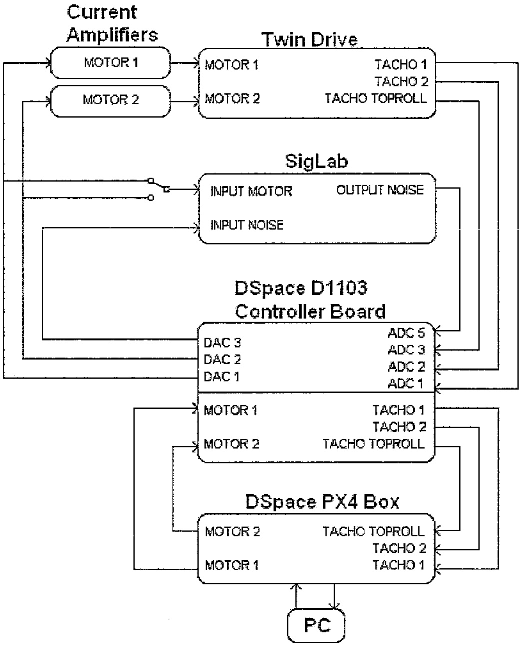
Current Amplifiers
MOTOR 1
MOTOR 2
Twin Drive
MOTOR 1
MOTOR 2
TACHO 1
TACHO 2
TACHO TOPROLL
SigLab
INPUT MOTOR
INPUT NOISE
OUTPUT NOISE
DSpace D1103 Controller Board
DAC 3
DAC 2
DAC 1
ADC 5
ADC 3
ADC 2
ADC 1
MOTOR 1
MOTOR 2
TACHO 1
TACHO 2
TACHO TOPROLL
DSpace PX4 Box
MOTOR 2
MOTOR 1
TACHO TOPROLL
TACHO 2
TACHO 1
PC

Figure 3.8: SigLab measurement

3.5.1 Case I

The first FRF that has been measured is from the input of motor 1 to the velocity of the roll of motor 1, without the belt, see Figure 3.6 case I. With this FRF the model of the motor can be validated. The measured FRF of motor 1 is given in Figure 3.9.

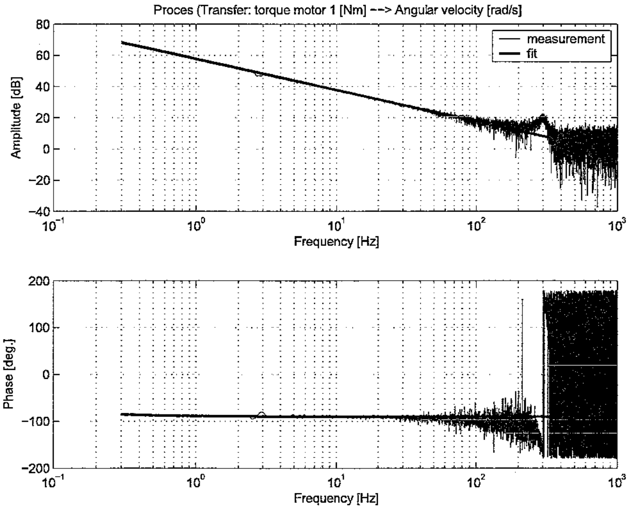

Figure 3.9: Bode plot of motor 1

In this figure the proposed model defined in equation 3.7 has been inserted with the values of J and d given in section 3.4. It can be concluded that the inertia is estimated satisfactory. To obtain a reliable estimation of the damping, the measurement should be done longer to get a better view on the low frequent area. The resonance peek at 300 $[Hz]$ shows that at this frequency the tacho starts to uncouple. The bode plot of motor 2 can be found in Appendix B.5. Here similar results hold.

3.5.2 Case II

Now the belt is wrapped around the two lower rolls and all four transfers have been measured, see Figure 3.6 case II. The references during the FRF measurements are constant velocities, in order to prevent the system from getting in the dry friction area. When driving the system at different jog modes, the strains in the belt parts between the rolls change caused by the stress acting on these belt parts. The dynamic behaviour of the belt parts is assumed to be strain dependent which will be explained at the end of this section. These dynamics are visualized for rotational speeds of the jog modes of 30, 60 and 80 $[rad/s]$.

The FRF's from input of the motors to the velocities of the motors have been measured in DSpace. Figures 3.10 and 3.11 show the transfer functions from input of motor 1 to the position of motor 1 (H_{11}) and from input of motor 1 to the position of motor 2 (H_{12}) with the three jog modes.

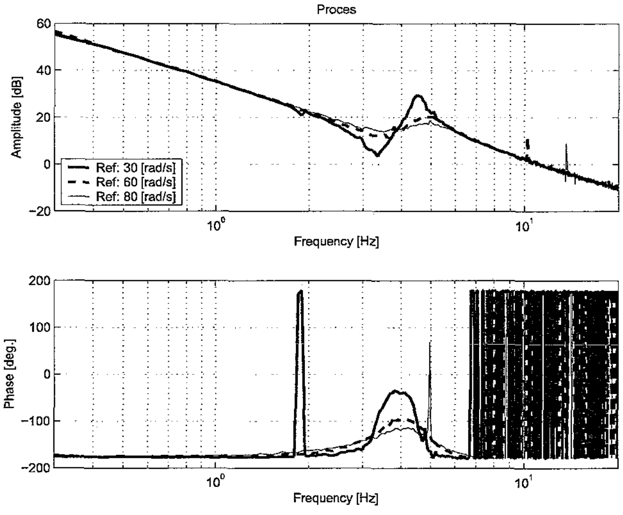

Figure 3.10: Measured transfer H_{11}

Figure 3.10 shows an antiresonance followed by a resonance. The antiresonance peak is caused by motor 2 that is in the opposite phase creating the same amount of torque as the actuator, whereas the resonance peak is the result of the system being in its natural frequency. For low frequencies the process can be approximated as a rigid body. The mass of the rigid body is the sum of the inertias of motor 1 and 2. For high frequencies again a rigid body approximation can be made. Here, the mass equals the inertia of motor 1. Motor 2 has

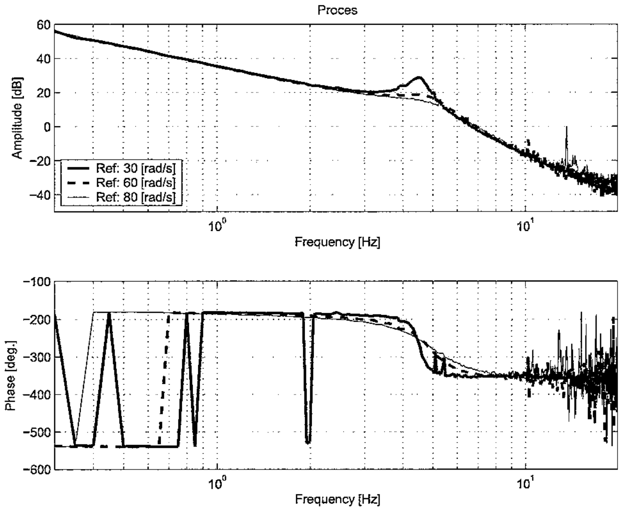

Figure 3.11: Measured transfer H_{12}

been uncoupled. Figure 3.11 only shows a resonance peek. In lower frequency regions the system behaves as a rigid body. For high frequencies, the limited stiffness of the belt causes motor 2 to decouple resulting in a -4 slope. When controlling this process, the bandwidth is limited by the resonance, as a phase loss of 180 degrees occurs. Therefore the bandwidth of the measurement with SigLab is chosen at frequencies of interest, upto 20 $[Hz]$. The transfer functions from motor 2 to the position of motor 2 and the position of motor 1 are similar to the ones above, because of the symmetry of the system, and are given in Appendix B.5.

A conclusion that can be drawn from these figures is that the damping of the resonance peek increases with the rotational velocity. When increasing the speed, the difference between the strains in the two belt parts increases. This causes a larger slip on the rolls. Slipping over the rolls causes the belt elements start to warm up and lead to energy loss, which can be seen as some sort of damping. The stiffness between the two rolls does not change when driving the system at different angular velocities. The reason for this is that the total stiffness originates from two parallel springs. Driving the system at a higher angular velocity causes one spring to get stiffer and the other to get weaker but the resultant stiffness remains unchanged.

3.5.3 Case III

The last two transfer functions that have been measured are the transfer functions from the motors to the position of the toproll, see Figure 3.6 case III. Different dynamic behaviour occurs when driving the system in the two directions. This is again caused by the different strains and tensions that are present in the different belt elements. The slipping behaviour as described at the end of section 3.5.2 is also present in this situation. Also the stiffness of the belt parts vary as will be explained later in this section.

The FRF of the input of motor 1 to the position of the toproll for both directions are given in Figure 3.12 and Figure 3.13.

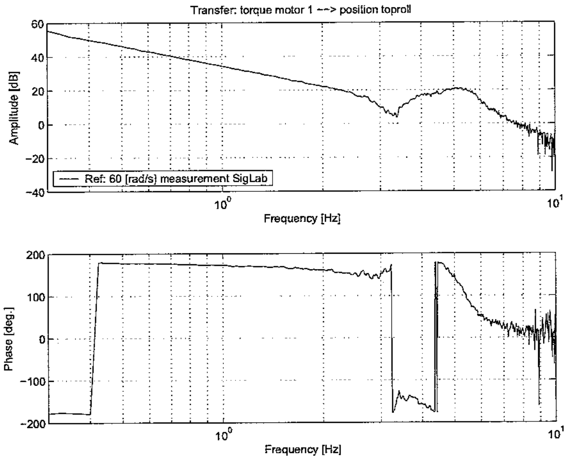

Figure 3.12: Measured transfer: motor 1 to toproll, clockwise

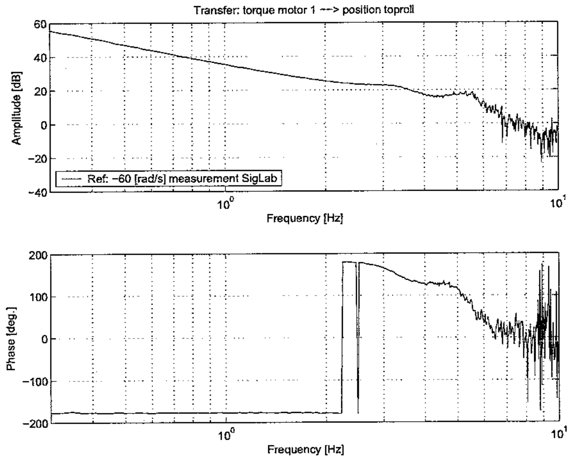

Figure 3.13: Measured transfer: motor 1 to toproll, counter clockwise

As expected the transfer functions for both directions are not equal. The damping and stiffness of the belt elements vary with the strain in the belt parts. For the clockwise situation (see Figure 3.15), the belt part between the rolls of motor 1 and motor 2 contains the largest tension and therefore the largest strain. The lowest strain and tension is present in the belt part between the toproll and the roll of motor 1. From these measured FRF's together with the model (see figure 3.14) it can be concluded that for the clockwise situation the following inequality holds:

$$k_{12} > k_{23} > k_{13} \tag{3.10}$$

For the counter clockwise situation (see Figure 3.15), the same sort of reasoning holds from which it can be concluded that:

$$k_{13} > k_{23} > k_{12} \tag{3.11}$$

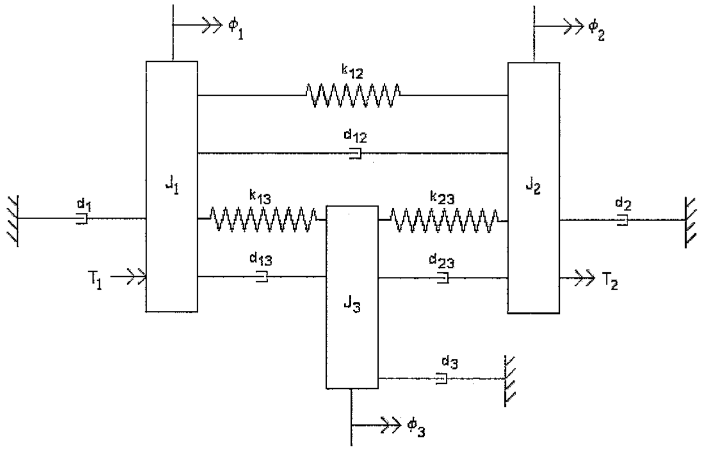
ϕ_1
ϕ_2
k_{12}
d_{12}
J_1
J_2
k_{13}
k_{23}
d_1
d_2
T_1
T_2
d_{13}
d_{23}
J_3
d_3
ϕ_3

Figure 3.14: Sixth order model

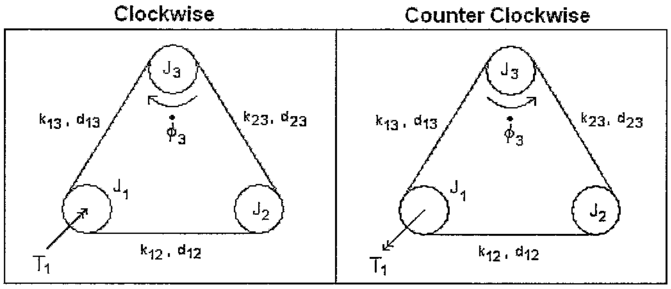
Clockwise
Counter Clockwise
J_3
k_{13}, d_{13}
$\dot{\phi}_3$
k_{23}, d_{23}
J_1
J_2
T_1
k_{12}, d_{12}

Figure 3.15: Clockwise versus counter clockwise

For motor 2 these transfer functions have also been measured (see Appendix B.5). It can be concluded that symmetry holds in this system. Driving the toproll in positive direction by motor 1 shows the same transfer function as driving the toproll in negative direction by motor 2.

3.6 Conclusions

In this chapter the tachos are calibrated and the motor constants were determined. The inertia, coulomb and viscous coefficients were estimated using step responses. Finally, transfer functions were determined for three cases in different jog modes. It was experienced that the dynamics of the system strongly depends on the belt velocity. In the next chapter, the control design will be presented.

Chapter 4

Control Design

Now that a plant model is obtained, model based control becomes possible. This chapter will discuss the control of the Twin Drive, focussed on the actuation system. Therefore, the four measured FRF's of case II (see Figure 3.6) have been fitted. The fits are based on a linearized model around a working point. A modal analysis can be performed from which the system is transformed into natural coordinates instead of physical coordinates leading to a modal decoupling of the dynamics. In order to quantify the residual non-diagonal terms compared to the diagonal terms the relative gain array (RGA) will be computed [Sko96]. In this way, two separate SISO controllers are designed to control the Twin Drive. For stability of the total system the Generalized Nyquist stability criterion is used [Macie89], which can be controlled individually by the two SISO controllers.

4.1 Model Fitting

In this section a linear model is fitted on the measured transfers of case II. The proposed model is derived in Appendix A.1. The four transfer functions given in equations A.3 through A.6 are fitted manually on the experimental data. The values of the parameters J_1, J_2, d_1 and d_2 used for these fits, are given in section 3.4. The values for d_{12} and k_{12} are adjusted such that the error between the experimental data and the fit is minimal. The determined values are $5.2 \cdot 10^{-4}$ $[Nms/rad]$ for d_{12} and $7.5 \cdot 10^{-2}$ $[N/rad]$ for k_{12}. The result of these fits are given in Figure 4.1.
The dynamics of the system can be describes as

$$\underline{M}\underline{\ddot{q}} + \underline{D}\underline{\dot{q}} + \underline{K}\underline{q} = \underline{Q} \tag{4.1}$$

where the matrices $\underline{M}$, $\underline{D}$, $\underline{K}$ are the mass, damping and stiffness matrix which are known.

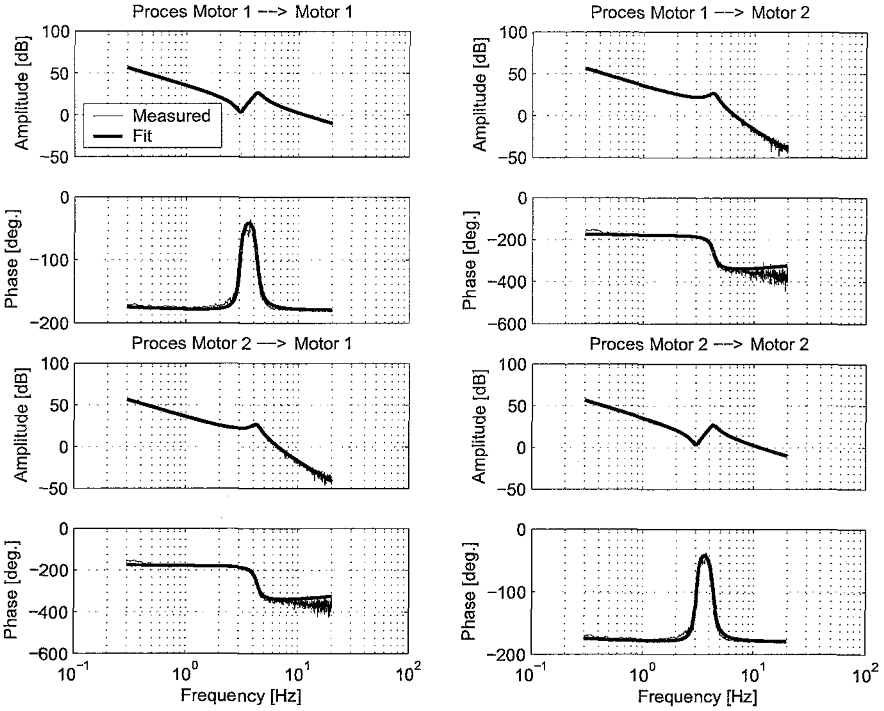

Figure 4.1: Four fits on experimental data

4.2 Modal Analysis

Now the modal analysis can be done [Kra00]. The idea of the modal analysis is to find the eigenvalues and the eigencolumns which can be used to transform the system in modal coordinates $\underline{\eta}$ instead of the physical coordinates $\underline{q}$. If the system, written in natural coordinates, has diagonal mass, damping and stiffness matrices, the system is decoupled.
First the eigenvalue problem (4.2) must be solved in order to obtain the eigenvalues and eigencolumns.

$$\left[\underline{K} - \omega^2 \underline{M}\right] \underline{u} = \underline{0} \tag{4.2}$$

leading to the eigenvalues

$$\begin{aligned} f_1 &= 0\ [Hz] \\ f_2 &= 4.32\ [Hz] \end{aligned} \tag{4.3}$$

and the modal matrix

$$\underline{U} = \left[\begin{array}{cc} -49.5317 & -49.2965 \\ -49.5317 & 49.7680 \end{array} \right]. \tag{4.4}$$

From the above results it can be concluded that a rigid body mode ($f_1 = 0[Hz]$) is present.

4.3 Modal Decoupling

With the columns of $\underline{U}$ found in section 4.2 the transformation from generalized, physical coordinates to natural coordinates can be achieved, so that:

$$\underline{q} = \underline{U}\underline{\eta} \tag{4.5}$$

Combining this within the equations of motion 4.1 and defining $\lceil m_r \rfloor = \underline{U}^T \underline{M} \underline{U}$ as the normalized mass-matrix and $\lceil k_r \rfloor = \underline{U}^T \underline{K} \underline{U}$ as the normalized stiffness-matrix, we obtain

$$\lceil m_r \rfloor \ddot{\underline{\eta}} + \underline{U}^T \underline{D} \underline{U} \dot{\underline{\eta}} + \lceil k_r \rfloor \underline{\eta} = \underline{N} \tag{4.6}$$

where

$$\underline{N} = \underline{U}^T \underline{Q} \tag{4.7}$$

is a column of generalized forces associated with the column of generalized coordinates η.
If the matrix $\underline{U}^T \underline{D} \underline{U}$ is diagonal then this particular case has proportional damping and the equations of motions are decoupled. However here we are dealing with a non-proportional damping. The calculated matrix $\underline{U}^T \underline{D} \underline{U}$ is:

$$\underline{U}^T \underline{D} \underline{U} = \begin{bmatrix} 0.1946 & -0.0323 \\ -0.0323 & 5.2981 \end{bmatrix} \tag{4.8}$$

Further analysis of whether or not the system can be decoupled is necessary. For weakly damped systems, dimensionless modal damping factors ξ_r can be calculated:

$$\xi_r = \frac{d_r}{2\omega_r m_r} = \frac{d_r}{2\sqrt{k_r m_r}} \tag{4.9}$$

The value for ξ_2 is 0.09 which is $\ll 1$. Therefore an approximated system is reconstructed ignoring the present non-diagonal terms of the matrix $\underline{U}^T \underline{D} \underline{U}$ and only using the diagonal terms of $\underline{U}^T \underline{D} \underline{U}$,

$$\underline{U}^T \underline{D} \underline{U} \approx \begin{bmatrix} 0.1946 & 0 \\ 0 & 5.2981 \end{bmatrix} = \lceil d_r \rfloor \tag{4.10}$$

so that

$$\underline{D}^\star = \underline{U}^{-T} \lceil d_r \rfloor \underline{U}^{-1} \tag{4.11}$$

which equals

$$\underline{D}^\star = 1 \cdot 10^{-3} \begin{bmatrix} 0.5599 & -0.5200 \\ -0.5200 & 0.5595 \end{bmatrix} = \begin{bmatrix} d_1^\star + d_{12}^\star & -d_{12}^\star \\ -d_{12}^\star & d_2^\star + d_{12}^\star \end{bmatrix} \tag{4.12}$$

This approximated system and the actual system are given in the Appendix figure C.1. It can be concluded that the approximation is satisfactory.

The 2x2 MIMO system is described as:

$$\underline{q} = \begin{bmatrix} H_{11} & H_{12} \\ H_{21} & H_{22} \end{bmatrix} \underline{Q} = \underline{PQ} \tag{4.13}$$

which is strongly coupled, see also figure 4.1. Transforming the input ($\underline{q} = \underline{U\eta}$) and the output ($\underline{Q} = \underline{U}^{-T}\underline{N}$) the system in modal coordinates becomes:

$$\underline{U}^{-1}\underline{PU}^{-T} = \underline{P_{modal}} \tag{4.14}$$

which is approximately decoupled, see figure 4.2.

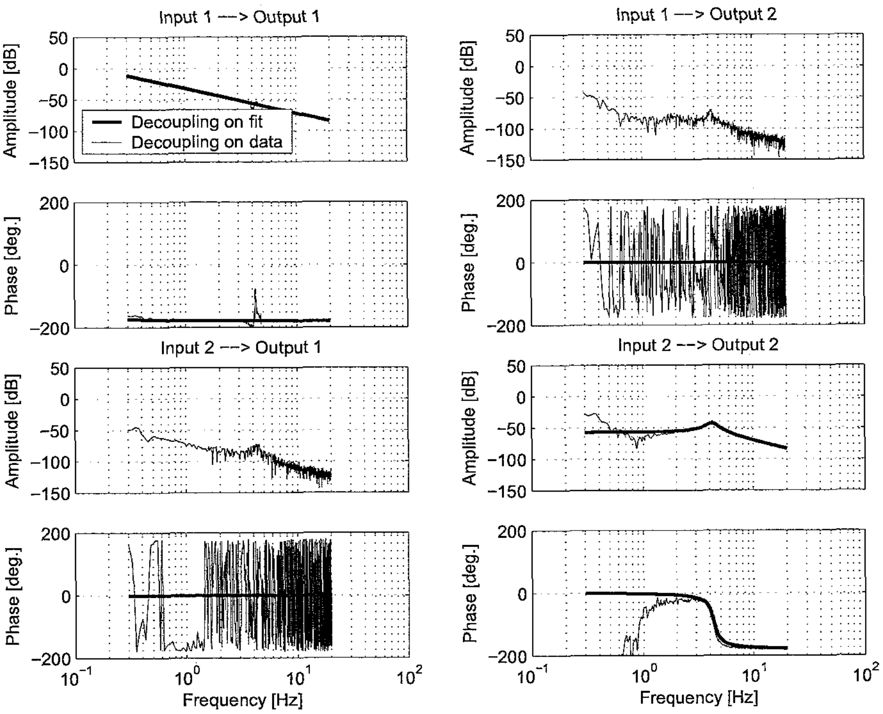

Figure 4.2: Decoupled system

The H_{11} term shows a rigid body mode, whereas the H_{22} term shows a flexible mode. The non-diagonal terms should be zero in case of perfect decoupling. Nevertheless, these terms are not zero. In order to quantify the residual non-diagonal terms compared to the diagonal terms the relative gain array (RGA) has been computed [Sko96].

The relative gain array of a non-singular square matrix $\underline{G}$ is a square matrix defined as

$$RGA(\underline{G}) = \underline{\Lambda}(\underline{G}) \triangleq \underline{G} \times (\underline{G}^{-1})^T \tag{4.15}$$

where × denotes element-by-element multiplication. When the RGA for each frequency equals the identity matrix, the system is said to be diagonal dominant. The RGA per frequency is given in figure 4.3.

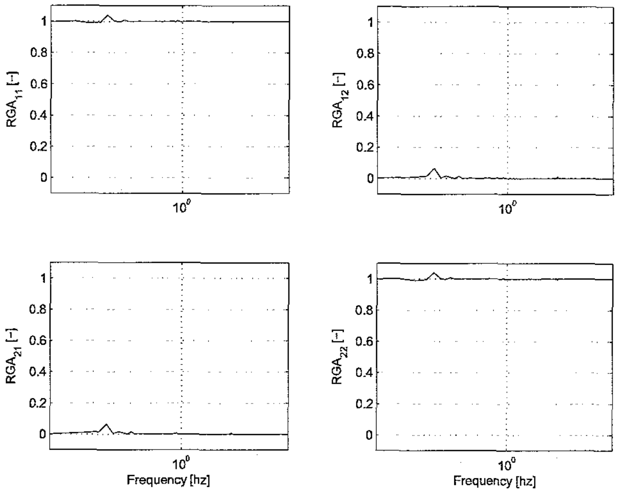

Figure 4.3: RGA

From this figure it can be concluded that the diagonal terms dominate for every frequency and the system has little coupling. Hence, the MIMO system can be considered as two independent SISO systems . Therefore, modal decoupling is satisfactory.

4.4 Control Design

Now that the system has been transformed in modal coordinates, the next step is to control the system. Since the system is decoupled this implies that two separate SISO controllers can be designed. The control scheme of controlling the physical coordinates $\underline{q}$ is given in figure 4.4.

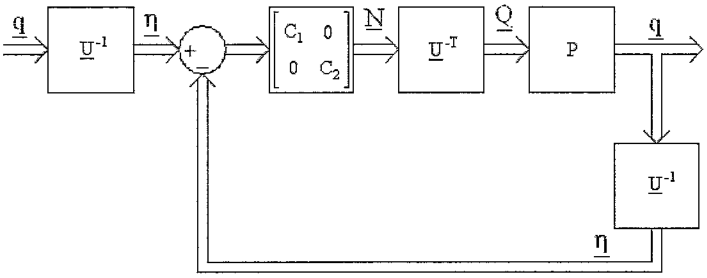

Figure 4.4: Control scheme

To control the system two lead lag filters have been designed to obtain crossover frequencies of 10 $[Hz]$. The parameters of these controllers can be found in Appendix C. The openloop of the system using these controllers is given in Figure 4.5.

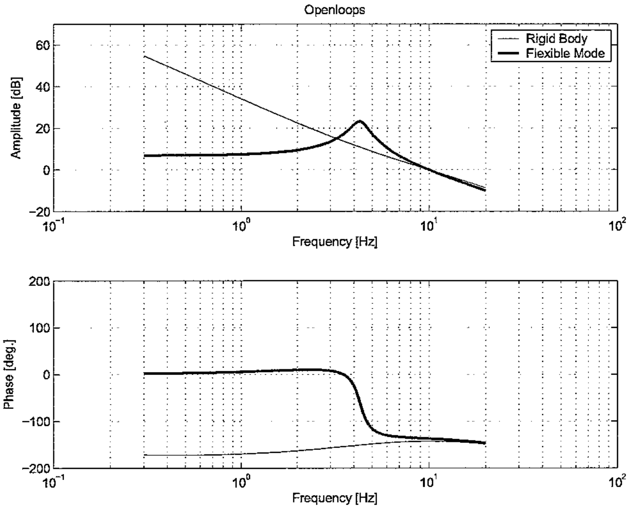

Figure 4.5: Openloops using fitted processes (BW = 10 $[Hz]$)

To obtain insight in the stability of the total system the generalized Nyquist stability criterion is used [Macie89]. We define the characteristic loci λ_i of the transfer function matrix $G(s)$ to be the eigenvalues of $G(j\omega_i)$ plotted per frequency ω_i. For these characteristic loci the following theorem holds:

Theorem 1 (Generalized Nyquist criterion) *If $G(s)$ has p_0 unstable (Smith-McMillan) poles, then the closed-loop system with return ratio -$kG(s)$ is stable if and only if the characteristic loci of $kG(s)$, taken together, encircle the point -1 p_0 times anti-clockwise, assuming that there are no hidden modes.*

The two loci have to pass the point (-1,0) at the right side, with sufficient amplitude- and phase margins. Due to decoupling the characteristic loci of the system can now be controlled independently with the controllers C_1 and C_2 (see Figure 4.4). With SISO loopshaping techniques the stability of the MIMO system can now directly be achieved. The characteristic loci of the controllers on the linear model are given in Figure 4.6. The characteristic loci on experimental data are given in Appendix C. The amplitude margins can not exactly be read from this figure but are at least 4, i.e. ≈ 12 $[dB]$ for both the characteristic loci and the phase margin is 37 $[deg.]$ for the rigid body mode and 43 $[deg.]$ for the flexible mode. Hence, the system is stable.

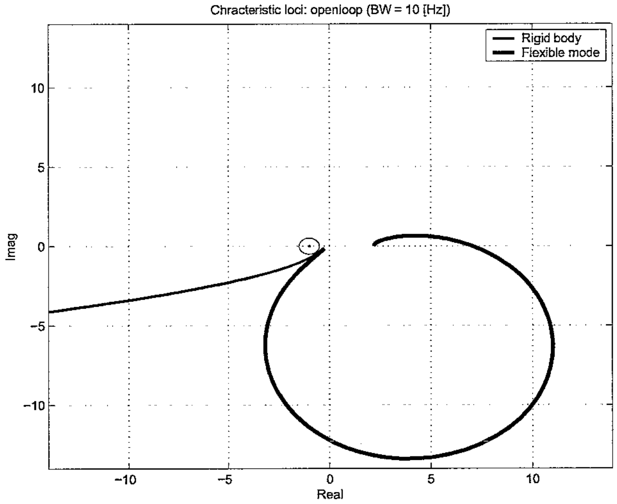

Figure 4.6: Characteristic loci openloop (BW = 10 $[Hz]$)

The sensitivity has been measured to derive the openloop FRF of the system, see Figures 4.7 and 4.8. Because of the high bandwidth of the closed loop system, identification of the process at higher frequencies becomes possible (see Appendix C). The non-diagonal terms are very small, attempts to measure the non-diagonal terms fail because of the low coherence.

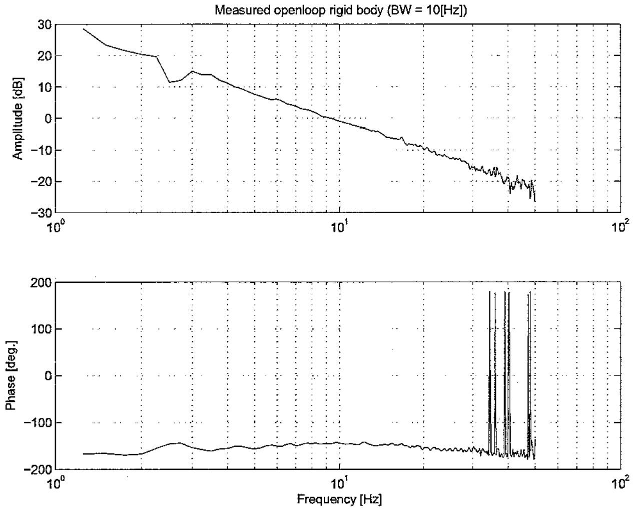

Figure 4.7: Measured open loop rigid body (BW = 10 $[Hz]$)

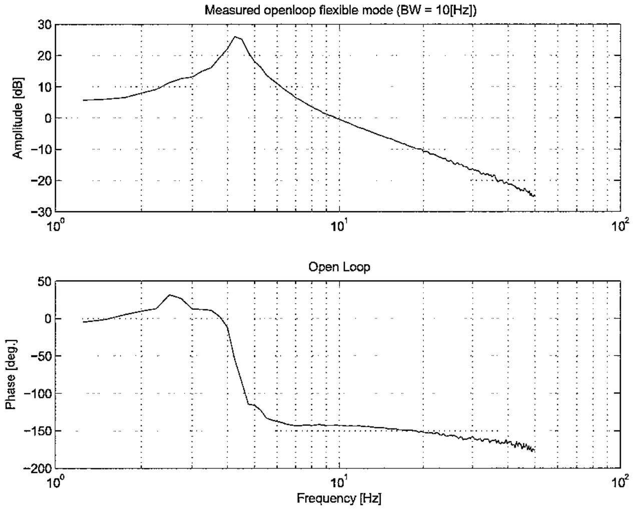

Figure 4.8: Measured open loop flexible mode (BW = 10 $[Hz]$)

With the new measured processes new controllers were designed to obtain a higher bandwidth. A bandwidth of 30 [*Hz*] has been chosen (see figure 4.9). The amplitude margins are at least 12 [*dB*] and the phase margin of the rigid body is 50 [*deg.*] and 48 [*deg.*] for the flexible mode.

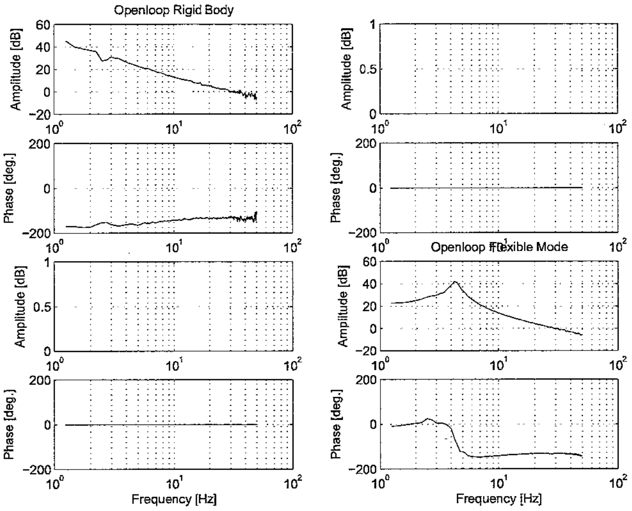

Figure 4.9: Openloops using measured processes (BW = 30 [*Hz*])

From the characteristic loci given in Appendix C.9 it can be seen that the system is stable. Again the controllers have been validated by measuring the sensitivity and calculating the openloop (see appendix C).

4.5 Conclusions

During this chapter the experimental data is fitted. A modal analysis has been carried out and leads to a modal decoupling of the actuation system of the Twin Drive. After decoupling the Relative Gain Array (RGA) has been calculated which points out strong diagonal dominance of the decoupled system. With the decoupled system separate SISO controllers have been designed which lead to a higher bandwidth then without decoupling. For stability the characteristic loci are plotted and examined to the generalized Nyquist criterium. The controllers have been validated by measuring the sensitivities from which the plant is identified at even higher frequencies.

Chapter 5

Conclusion and Recommendations

5.1 Conclusions

In this section, conclusions of the work are presented. The following problem statement was formulated:

Problem statement

> Is it possible to decouple the dynamics of the Twin Drive and can controllers be designed for this decoupled system?

The following conclusion can be drawn concerning this problem statement:

Main conclusion

> The dynamics of the actuation system of the Twin Drive have been described in modal coordinates and resulted in a diagonal dominant decoupled system. Separate SISO controllers are designed which lead to a higher bandwidth then was possible without decoupling.

The system identification is discussed and after that the control design is considered.

System Identification

First the system is calibrated and system parameters are identified. Frequency response functions have been measured in various cases around several working points to obtain insight in the dynamics of the Twin Drive.

Control Design

Fits were made on the experimental data of the actuation system using linearized models. With the results of these fits a modal analysis has been carried out, in order to decouple the Twin Drive. The RGA analysis shows that after the modal decoupling there is diagonal dominance. Two controllers are designed with bandwidths of 10 and 30 $[Hz]$. These bandwidths are higher than the systems first resonance frequency.

5.2 Recommendations

Several aspects have been investigated in this work. Still a lot can be investigated. Therefore the following recommendations are made:

- During this work it becomes clear that the dynamics have a non-linear behaviour. Here, around three working points with different velocities linearizations have been made. One could derive models where the parameters are dependent on the velocities.
- Belt drives are subjected to sliding wear as the belt creeps against the pulley during tensions transitions. The sliding of the belt is a phenomenon that also plays part in this setup. Several models have been derived for these sliding belts, for example see [Lea02]. The slip on the rolls causes the belt to warm up and lead to energy loss, which can be seen as some sort of damping. More slip of the belt leads to more damping in the belt parts. With the models an insight in the slip phenomenon can be obtained.
- At last, a new challenge is to control the velocity of the toproll together with the belt tensions by means of the two motors that can be actuated. Before this can be investigated the measurement of the load cell must be made accessible.

Appendix A

Linearized Models

To provide insight in the dynamics of the Twin Drive linear models have been derived. These models have been fitted on the experimental data. Two models have been derived:

- a fourth order model in case the belt is wrapped around the two lower rolls (Case II)
- a sixth order model in case the belt is wrapped around all three rolls (Case III)

A.1 Fourth Order Model

In case the belt is wrapped around the rolls of motor one and motor two the following model is derived:

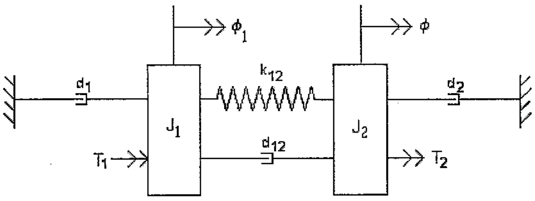

Figure A.1: Fourth order model

By defining

$$\underline{q} = \begin{bmatrix} \phi_1 \\ \phi_2 \end{bmatrix} \tag{A.1}$$

the equations can be written in the form

$$\underline{M}\ddot{\underline{q}} + \underline{D}\dot{\underline{q}} + \underline{K}\underline{q} = \underline{Q} \tag{A.2}$$

with

$$\underline{M} = \begin{bmatrix} J_1 & 0 \\ 0 & J_2 \end{bmatrix} \quad \underline{B} = \begin{bmatrix} d_1 + d_{12} & -d_{12} \\ -d_{12} & d_2 + d_{12} \end{bmatrix}$$

$$\underline{K} = \begin{bmatrix} k_{12} & -k_{12} \\ -k_{12} & k_{12} \end{bmatrix} \quad \text{and} \quad \underline{Q} = \begin{bmatrix} T_1 \\ T_2 \end{bmatrix}$$

The individual transfer functions become

$$H_{11} = \frac{(J_2s^2 + (d_2 + d_{12})s + k_{12})}{s(q_1s^3 + q_2s^2 + q_3s + q_4)} \tag{A.3}$$

$$H_{12} = \frac{(d_{12}s + k_{12})}{s(q_1s^3 + q_2s^2 + q_3s + q_4)} \tag{A.4}$$

$$H_{12} = \frac{(d_{12}s + k_{12})}{s(q_1s^3 + q_2s^2 + q_3s + q_4)} \tag{A.5}$$

$$H_{22} = \frac{(J_1s^2 + (d_1 + d_{12})s + k_{12})}{s(q_1s^3 + q_2s^2 + q_3s + q_4)} \tag{A.6}$$

with

$$\begin{aligned} q_1 &= J_1J_2 \\ q_2 &= d_1J_2 + d_{12}J_2 + J_1d_2 + J_1d_{12} \\ q_3 &= d_1d_2 + d_1d_{12} + d_{12}d_2 + k_{12}J_2 + k_{12}J_1 \\ q_4 &= k_{12}d_1 + k_{12}d_2 \end{aligned}$$

A.2 Sixth order model

In case III, the belt is wrapped all rolls the following model is derived:

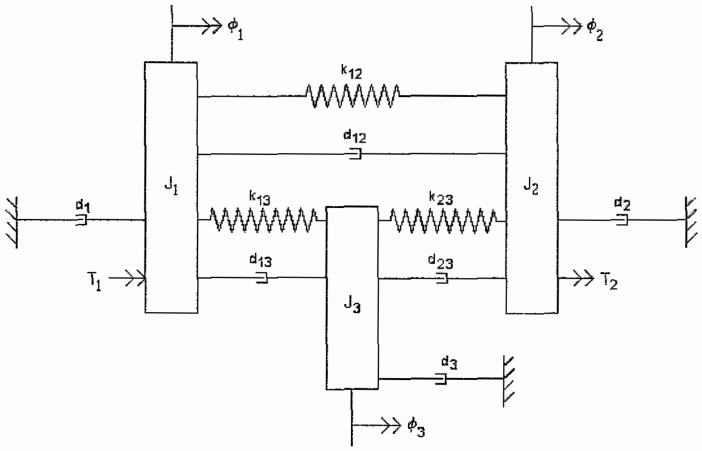

Figure A.2: Sixth order model

With the same derivation given in section A.1 and by defining

$$\underline{q} = \begin{bmatrix} \phi_1 \\ \phi_2 \\ \phi_3 \end{bmatrix} \tag{A.7}$$

this leads to

$$\underline{M} = \begin{bmatrix} J_1 & 0 & 0 \\ 0 & J_2 & 0 \\ 0 & 0 & J_3 \end{bmatrix} \quad \underline{B} = \begin{bmatrix} d_1 + d_{12} + d_{13} & -d_{12} & -d_{13} \\ -d_{12} & d_2 + d_{12} + d_{23} & -d_{23} \\ -d_{13} & -d_{23} & d_3 + d_{13} + d_{23} \end{bmatrix}$$

$$\underline{K} = \begin{bmatrix} k_{12} + k_{13} & -k_{12} & -k_{13} \\ -k_{12} & k_{12} + k_{23} & -k_{23} \\ -k_{13} & -k_{23} & k_{13} + k_{23} \end{bmatrix} \quad \text{and} \quad \underline{Q} = \begin{bmatrix} T_1 \\ T_2 \\ 0 \end{bmatrix}$$

Appendix B

Experimental Results

Here, experimental results are presented that are discussed in chapter 3.

B.1 Offset tachos

Here all measured offsets, that are discussed in section 3.1, are given:

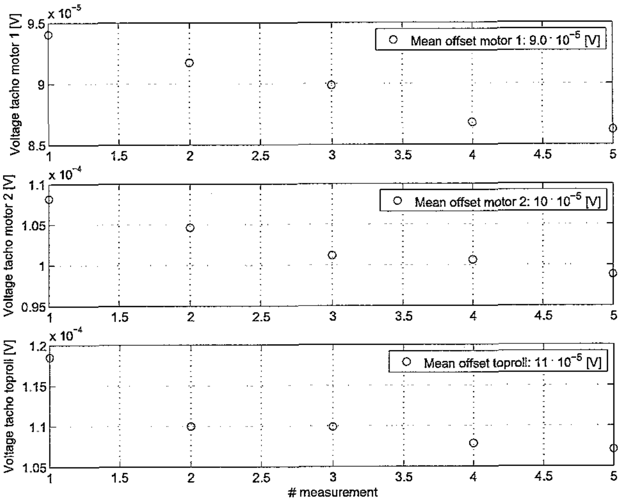

Figure B.1: Offsets of ADC's

B.2 Calibration tachos

In this section the results of the calibration of the tacho of motor 2 and the toproll are presented.

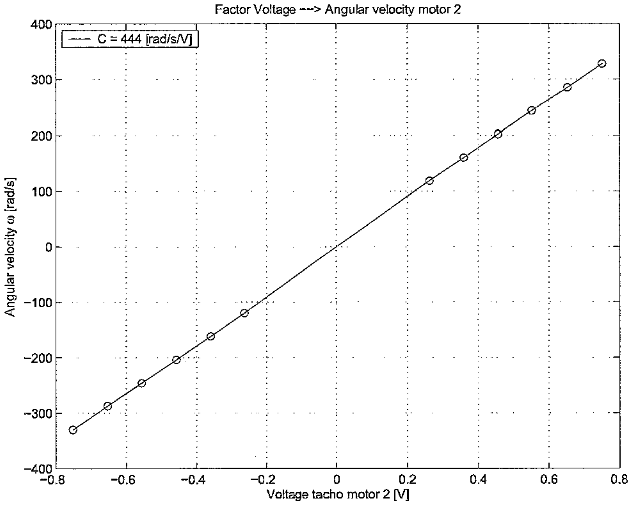

Figure B.2: Factor voltage to radians per second motor 2

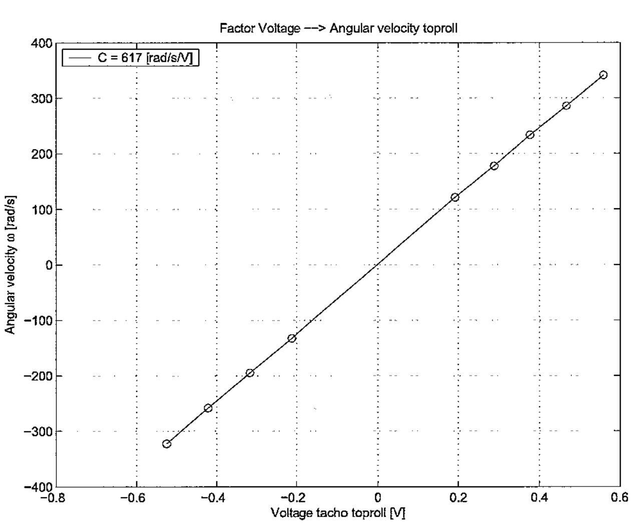

Figure B.3: Factor voltage to radians per second toproll

B.3 Motor constants

Here, the measured data for determining the motor constant of motor 2 is given:

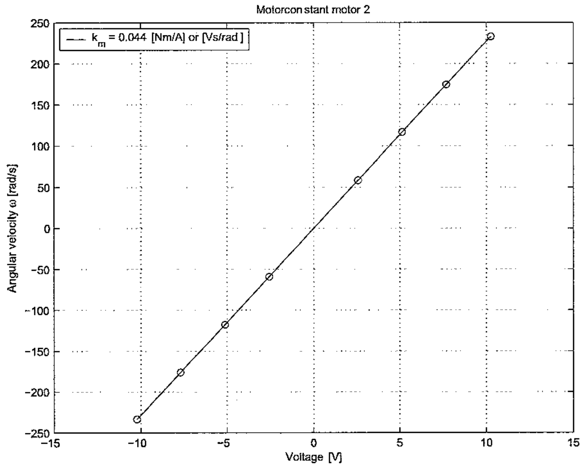

Figure B.4: Motor constant motor 2

B.4 Parameter estimation

Here, the estimated parameters of the inertia and the viscous damping factor of each step response are presented.
Inertia J motor 1:

$J \cdot 10^{-4}$	1	2	3	4	5	6	7	8	9	10
Step 1	2.2	2.0	2.0	2.0	2.0	2.1	1.9	1.9	1.9	1.9
Step 2	-	2.0	2.2	2.1	2.3	2.2	2.1	2.0	2.2	2.2
Step 3	2.0	1.8	2.0	1.9	2.5	2.1	1.5	2.3	2.0	2.2
Step 4	1.9	2.2	2.0	1.9	1.9	2.3	2.6	1.9	1.7	2.1

Table B.1: Values for inertia J motor 1

Viscous damping d motor 1:

$d \cdot 10^{-5}$	1	2	3	4	5	6	7	8	9	10
Step 1	3.4	3.5	3.5	3.9	3.8	3.8	3.6	4.1	4.0	4.0
Step 2	-	3.4	3.2	3.3	3.2	3.4	4.0	3.8	3.8	3.5
Step 3	2.4	2.9	2.4	2.6	2.5	4.0	3.6	3.8	3.3	3.6
Step 4	3.2	2.2	2.7	2.5	2.3	3.8	2.8	3.5	2.8	2.7

Table B.2: Values for viscous damping d motor 1

Inertia J motor 2:

$J \cdot 10^{-4}$	1	2	3	4	5	6	7	8	9	10
Step 1	1.8	1.9	1.8	2.1	1.6	1.7	1.8	2.4	2.0	1.9
Step 2	1.9	2.1	2.3	1.6	1.7	2.7	2.0	2.5	2.0	2.1
Step 3	2.5	2.0	1.8	2.2	2.1	1.8	1.6	1.8	2.0	2.0
Step 4	1.7	2.2	1.9	2.0	2.1	2.3	2.5	2.3	1.9	2.5

Table B.3: Values for inertia J motor 2

Viscous damping d motor 2:

$d \cdot 10^{-5}$	1	2	3	4	5	6	7	8	9	10
Step 1	5.6	5.6	7.4	8.7	6.5	4.3	5.5	5.1	5.8	5.9
Step 2	4.4	4.4	5.4	6.2	6.4	3.4	5.6	3.8	5.0	5.7
Step 3	2.8	4.4	5.3	4.5	4.0	4.7	3.6	4.5	3.3	2.6
Step 4	3.3	3.3	5.2	4.6	2.3	4.2	4.5	3.0	2.7	3.5

Table B.4: Values for viscous damping d motor 2

B.5 Frequency Response Functions

Transfer from the input of motor two to the velocity of motor one without belt:

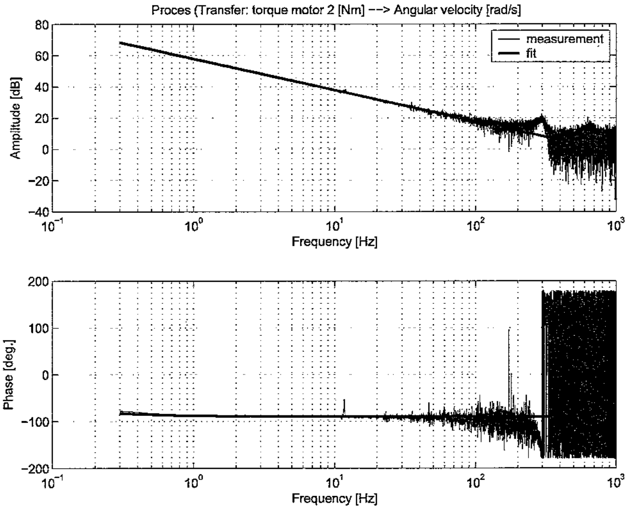

Figure B.5: Bode plot of motor 2

Transfer from the input of motor two to the position of motor one with the belt wrapped around motor one at jog modes of 30, 60 and 80 $[rad/s]$:

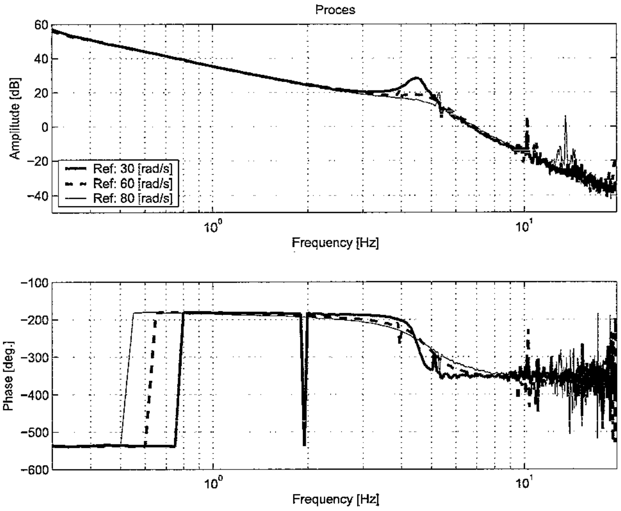

Figure B.6: Measured transfer H_{21}

Transfer from the input of motor two to the position of motor two with the belt wrapped around motor one at jog modes of 30, 60 and 80 $[rad/s]$:

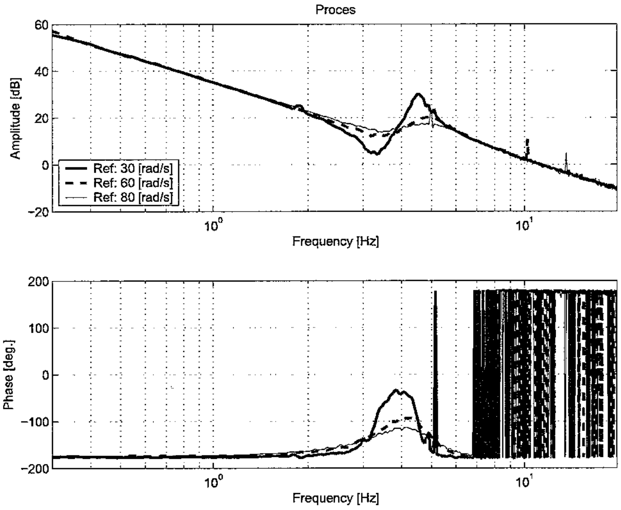

Figure B.7: Measured transfer H_{22}

Transfer from the input of motor two to the position of the toproll with the belt wrapped around the three rolls (positive direction):

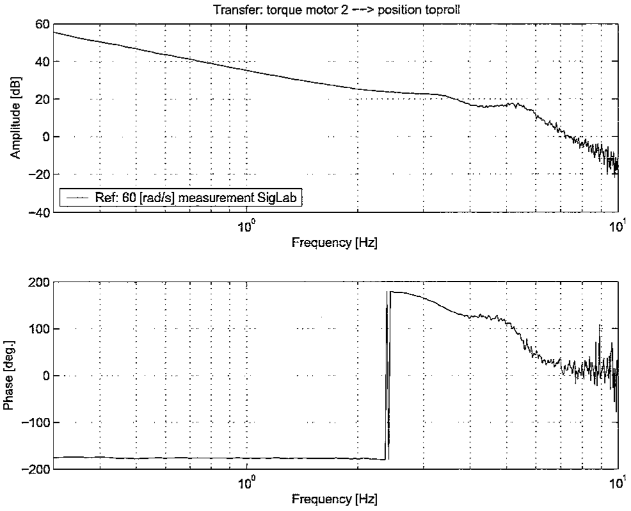

Figure B.8: Measured transfer: motor 2 to toproll, clockwise

Transfer from the input of motor two to the position of the toproll with the belt wrapped around the three rolls (negative direction):

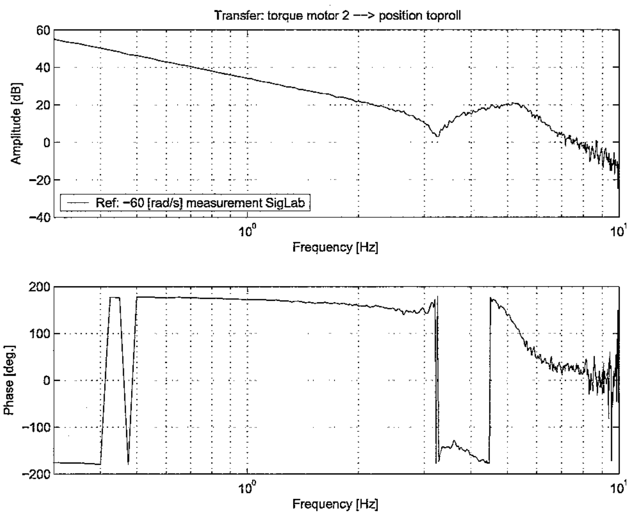

Figure B.9: Measured transfer: motor 2 to toproll, counter clockwise

Appendix C

Control Design

In the figure below the transfer functions are given in case of proportional and non-proportional damping (see section 4.3). From this figure it can be seen that the transfer functions are almost identical, so the proportional damping is a good approximation for the non-proportional case.

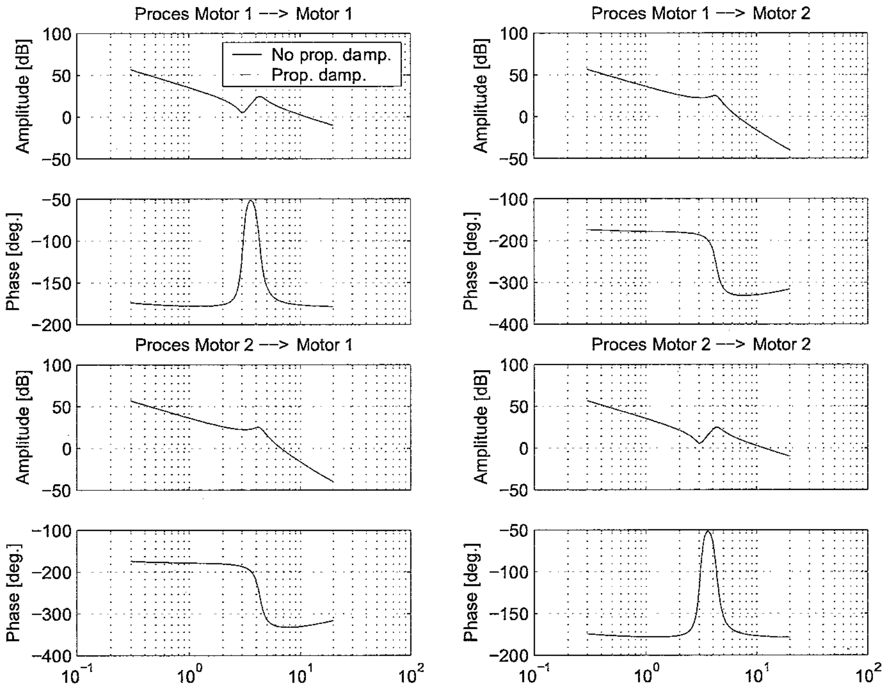

Figure C.1: Proportional damping versus non-proportional damping

Several SISO controllers have been designed in order to control the decoupled system. The parameters of these controllers that are used and discussed in 4 are given in this Appendix. The used controllers are all lead lag filters:

$$C = K\frac{\frac{1}{2\pi f_1}s+1}{\frac{1}{2\pi f_2}s+1} \tag{C.1}$$

After having designed the controllers a stability analysis has been done by studying the characteristic loci of the system. The characteristic loci of the experimental data are also given in this appendix.

First controllers were designed for a bandwidth of 10 $[Hz]$. The parameters defined in equation C.1 for these controllers are given below:

- Controller rigid body (BW = 10 $[Hz]$)
  - $K = 1.97 \cdot 10^3$
  - $f_1 = 1/2 \cdot 10$
  - $f_2 = 2 \cdot 10$
- Controller flexible mode (BW = 10 $[Hz]$)
  - $K = 1.61 \cdot 10^3$
  - $f_1 = 1/2 \cdot 10$
  - $f_2 = 2 \cdot 10$

The characteristic loci of the openloop using the controllers above is given in figure C.2.

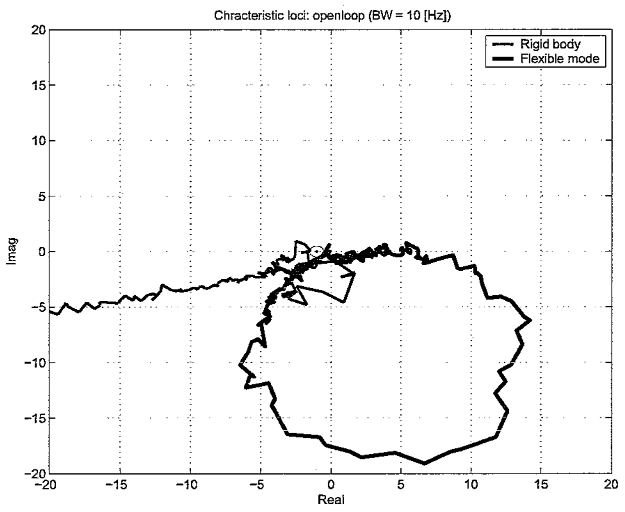

Figure C.2: Characteristic loci openloop (BW = 10 $[Hz]$)

Next, the sensitivities (see Figures C.3 and C.4) have been measured again to derive the openloops (see Figures C.5 and C.6).

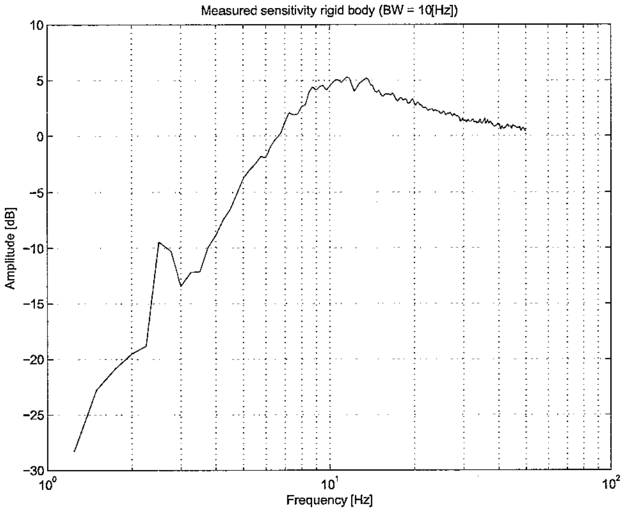

Figure C.3: Measured sensitivity rigid body using controller with BW of 10 $[Hz]$

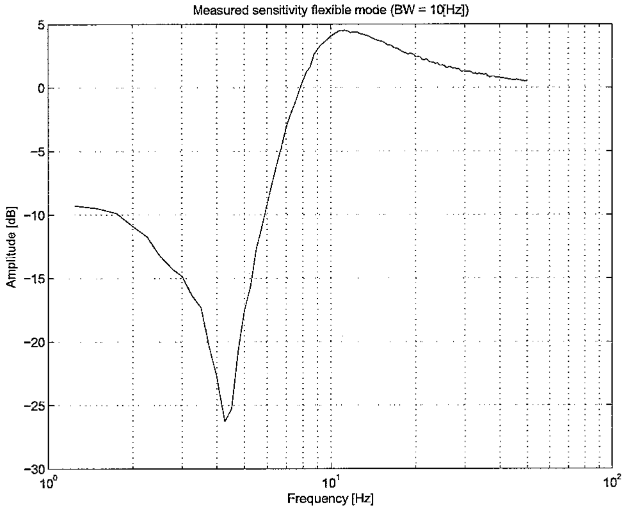

Figure C.4: Measured sensitivity flexible mode using controller with BW of 10 $[Hz]$

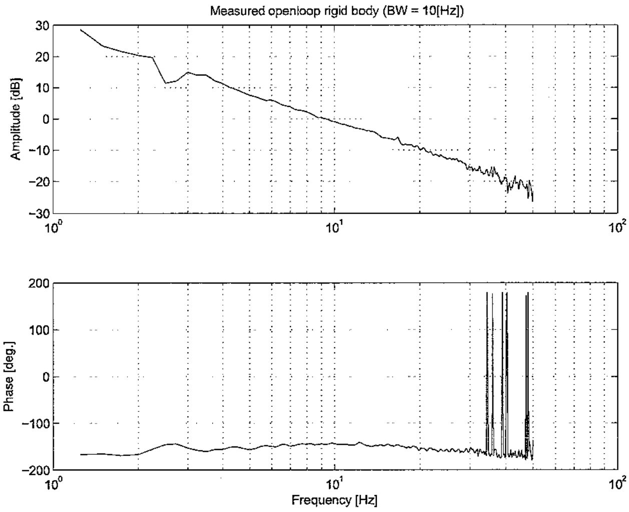

Figure C.5: Measured openloop rigid body using controller with BW of 10 $[Hz]$

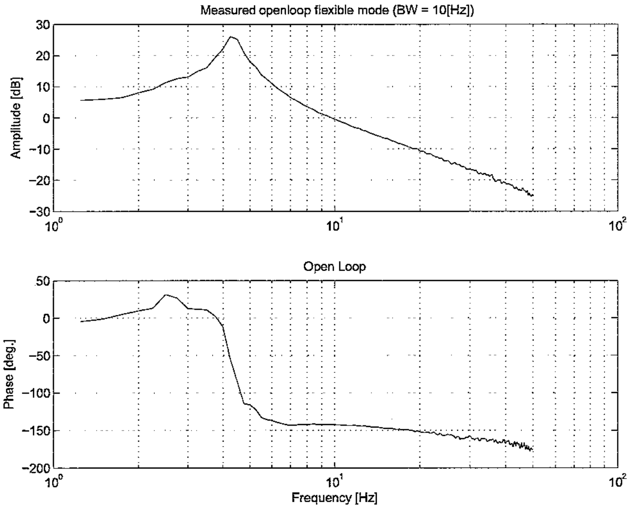

Figure C.6: Measured openloop flexible mode using controller with BW of 10 $[Hz]$

From these openloop the process has been derived (see Figures C.7 and C.8. The processes however have been identified in higher frequencies using a higher bandwidth of the SigLab measurement.

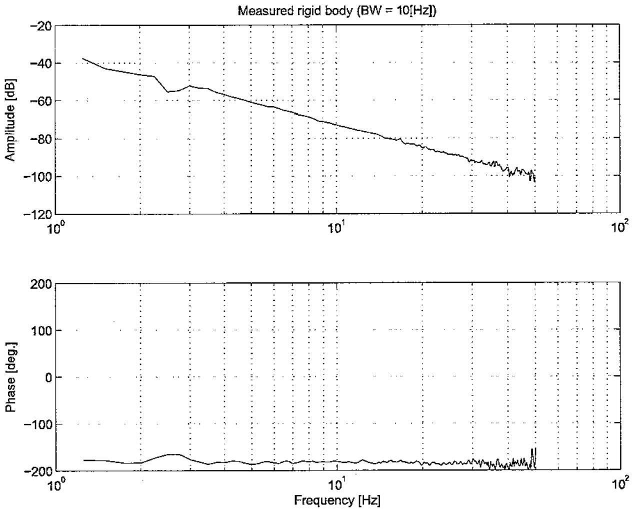

Figure C.7: Measured rigid body using controller with BW of 10 $[Hz]$

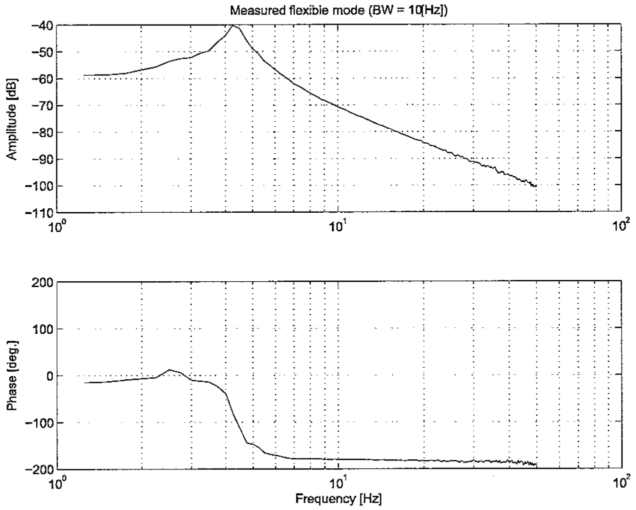

Figure C.8: Measured flexible mode using controller with BW of 10 $[Hz]$

Finally, controllers were designed for a bandwidth of 30 $[Hz]$. The parameters are given below:

- Controller rigid body (BW = 30 $[Hz]$)
  - $K = 1.38 \cdot 10^4$
  - $f_1 = 1/3 \cdot 30$
  - $f_2 = 3 \cdot 30$
- Controller flexible mode (BW = 30 $[Hz]$)
  - $K = 1.19 \cdot 10^3$
  - $f_1 = 1/3 \cdot 30$
  - $f_2 = 3 \cdot 30$

The characteristic loci of the openloop using the controllers above is given in figure C.9.

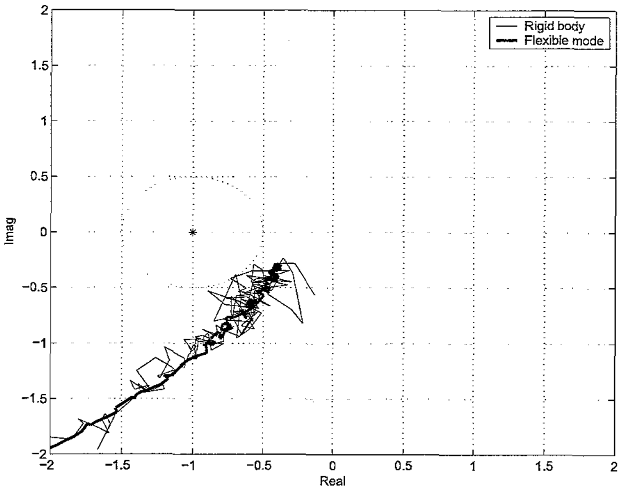

Figure C.9: Characteristic loci openloop (BW = 30 $[Hz]$)

Again, the sensitivities (see Figures C.3 and C.4) has been measured again to derive the openloop (see Figures C.5 and C.6).

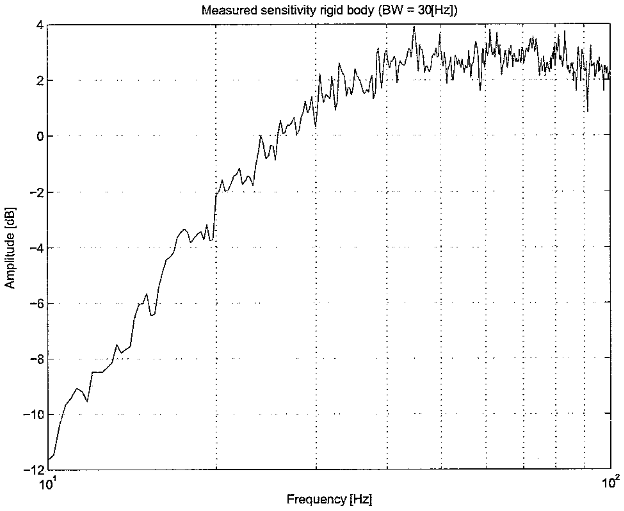

Figure C.10: Measured sensitivity rigid body using controller with BW of 30 $[Hz]$

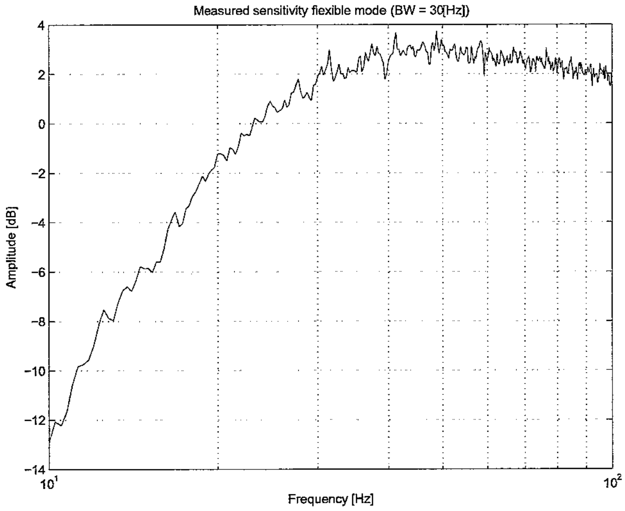

Figure C.11: Measured sensitivity flexible mode using controller with BW of 30 $[Hz]$

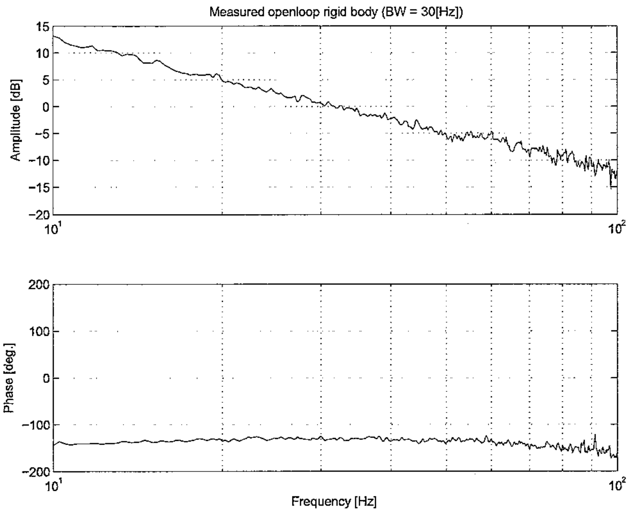

Figure C.12: Measured openloop rigid body using controller with BW of 30 $[Hz]$

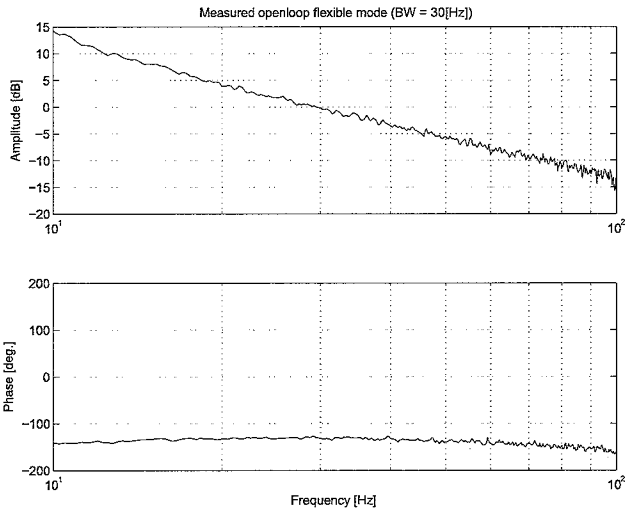

Figure C.13: Measured openloop flexible mode using controller with BW of 30 $[Hz]$

Bibliography

[Mohan02] N. Mohan, 'Electric Drives An Integrative Approach', pp. 7-13, 2002.

[Kra00] B. de Kraker, D.H. van Campen, 'Mechanical Vibrations', 2000.

[Macie89] J.M. Maciejowski, 'Multivariable Feedback Design', pp. 59-62, 1989

[Sko96] S. Skogestad, I. Postlethwaite, 'Multivariable Feedback Control Analysis and Design', pp. 86-91, 1996.

[Lea02] M.J. Leamy, T.M. Wasfy, 'Analysis of Belt-Drive Mechanics Using a Creep-Rate-Dependent Friction Law', Journal of Applied Mechanics, Vol. 69, pp. 763, 2002

[Pee04] M. Peeters, 'Exploratory study of the Twin Drive Rig', TU\e, DCT report no 2004.73, 2004.

[Har04] T. Hardemans, J. Schuurmans, 'Physical Model Of The Twin Drive Rig', Corus Research, Development and Technology, IJmuiden, 2004.